WPMST1-CPR(18) 18824

I. Paradela Perez et al.

Assessment of particle and heat loads to the upper open divertor in ASDEX Upgrade and comparison with SOLPS simulations

Preprint of Paper to be submitted for publication in Proceeding of 23rd International Conference on Plasma Surface Interactions in Controlled Fusion Devices (PSI-23)

This work has been carried out within the framework of the EUROfusion Consortium and has received funding from the Euratom research and training programme 2014-2018 under grant agreement No 633053. The views and opinions expressed herein do not necessarily reflect those of the European Commission.

Assessment of particle and heat loads to the upper open divertor in ASDEX Upgrade in favourable and unfavourable toroidal magnetic field directions

I. Paradela Pérez[a,b,*], M. Groth[a], M. Wischmeier[b], A. Scarabosio[b], D. Brida[b], P. David[b], D. Silvagni[b], D. Coster[b], T. Lunt[b], M. Faistch[b], the ASDEX-Upgrade Team[b], the EUROfusion MST1 Team[c]

[a] *Aalto University, Department of Applied Physics, Otakaari 1, 02150 Espoo, Finland*
[b] *See appendix of A. Kallenbach Nucl. Fusion 57 102015 (2017)*
[c] *See the author list of: H. Meyer et al. Nucl. Fusion 57 102014 (2017)*

Abstract

A database of pairs of ASDEX Upgrade L-mode shots with forward and reverse B_T directions has been used to study the role of drifts in the divertor dynamics and detachment physics. The evolution of the peak heat flux and the total power loads onto both the outer and the inner targets depends significantly on the toroidal field direction: increasing the core plasma density affects mainly the heat loads in the $B_T < 0$ direction whereas increasing the plasma current has a larger impact on the heat loads for $B_T > 0$. Ion saturation current measurements show similar trends to those of the IR data (different behaviour dependent on the field direction). These discrepancies are not only caused by drifts but also by different levels of radiated power. Tomographic reconstructions show that the power crossing the separatrix, P_{sep}, is not constant within the entire database. Finally, at $I_p = 0.8$ MA, the onset of power detachment is observed in both targets for both field directions. On the other hand, at $I_p = 0.6$ MA, the onset of power detachment is only observed for $B_T < 0$ at the outer target. Additionally, the onset of particle detachment is only observed at the outer target for $B_T < 0$ with $I_p = 0.8$ MA.

Keywords: ASDEX Upgrade, upper single null, scrape-off layer, SOLPS, divertor detachment

1. Introduction

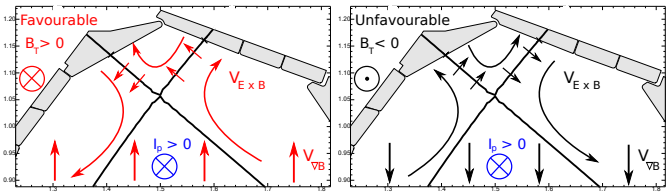

Figure 1: Drift velocity direction in USN configuration of AUG for (a) favourable and (b) unfavourable toroidal field direction.

Drifts are considered to play a critical role in the Scrape-Off Layer (SOL) and divertor transport and detachment. The onset of detachment is a reduction of particle and heat fluxes with respect to their maximum value. Understanding and controlling detachment is fundamental for the operational feasibility of future devices.

The flow pattern of the $V_{E\times B}$ and the $V_{\nabla B}$ drifts [1] for the two directions of the magnetic toroidal field is shown in Fig. 1.

The toroidal field direction in which the ion $V_{\nabla B}$ drift points towards the targets is called *favourable* ($B_T > 0$, Fig. 1 (a)). The opposite field direction is *unfavourable* ($B_T < 0$, Fig. 1 (b)).

Previous studies of the effect of drifts in different machines (AUG [2, 3, 4, 5], CMOD[1], JET [6], DIII-D [7], JT60-U [8]) reported similar observations with respect to the asymmetries of the inner and outer target temperatures and densities. In favourable field direction, a hotter, less dense outer target with respect to the inner target is usually observed, while in unfavourable field direction the asymmetry between inner and outer targets is reduced.

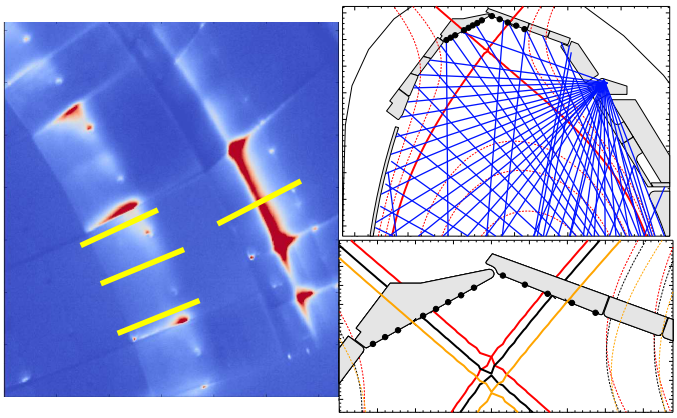

Figure 2: (a) profile lines of infrared thermography measurements, (b) bolometry lines of sight (LOS) and (c) strike point sweep and Langmuir probes location.

2. Experimental setup

A set of discharges were performed in the upper, open divertor of ASDEX Upgrade during its 2017 experimental cam-

*Corresponding author. *Email: ivan.paradela@ipp.mpg.de*

$\lvert B_T\rvert = 2.5\ T$						
$n_{H1}[10^{19}m^{-3}] =$		2.5	3.5	4.5	5.0	5.5
$I_p = 0.6\ MA$	$B_t < 0$	34303 34508	34623	–	–	–
	$B_t > 0$	34302	34624			
$I_p = 0.8\ MA$	$B_t < 0$	34314	34312	34505	34616	34503
	$B_t > 0$	34306	34311	34507	34618	–
$I_p = 1.0\ MA$	$B_t < 0$	34309	–	–	–	–
	$B_t > 0$	34308				

Table 1: Pairs of L-mode plasmas in forward and reverse toroidal field directions with different plasma conditions (plasma core density and current). Blue: $P_{ECRH} = 0.3$ MW instead of $P_{ECRH} = 0.5$ MW. Orange: No I_{sat} data. Red: No IR data.

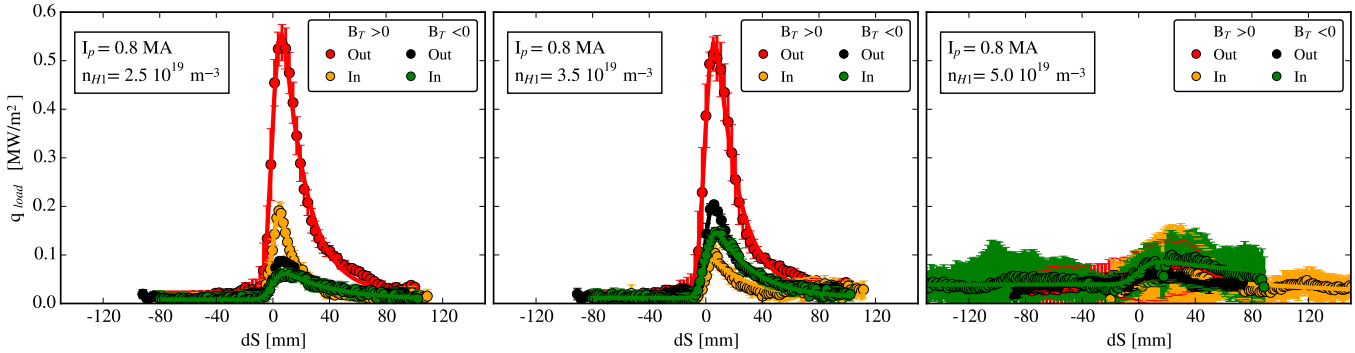

Figure 3: Heat flux deposition profiles as a function of the distance from the separatrix during the core plasma density scan with $I_p = 0.8$ MA.

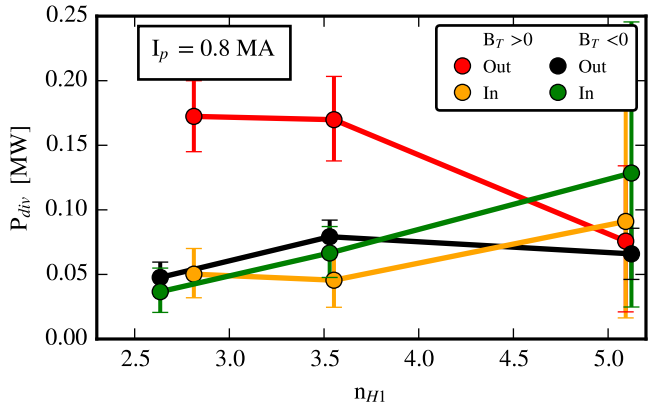

Figure 4: P_{div} as function of average core density, n_{H1}, for both toroidal field directions with $I_p = 0.8$ MA.

paign. The corresponding shot numbers are presented in Table 1. The database consists of pairs of shots in both toroidal field directions for which the same plasma conditions (plasma core density and current as well as input heating power) were maintained as similar as possible. The plasma core density is measured with the interferometer LOS H1. Although the toroidal field direction was reversed for half of the shots, the plasma current direction remained unchanged and thus the helicity was reversed.

The additional heating scheme consisted in Electron Cyclotron Resonance Heating (ECRH) delivering $P_{ECRH} = 0.5$ MW for all cases except those labelled with blue in Table 1, which only received $P_{ECRH} = 0.3$ MW. On top of that, three NBI blips were used at three different time points during the discharge in order to obtain Charge Exchange Recombination Spectroscopy (CXRS) measurements and delivered $P_{NBI} = 2.5$ MW with a blip duration of $\Delta t = 12$ ms. These NBI blips on top of the ECRH and the ohmic heating caused an L-H transition in some discharges, specially in favourable toroidal field direction. The occasional L-H fluctuations and the lack of a pumping system close to the upper divertor degraded the level of density control in some discharges.

Infra-red thermography provides the reconstruction of the heat flux onto the targets based on temperature measurements. Cameras capture the infra-red light emitted by the targets to infer their temperature [9]. Then, the heat flux distribution is calculated from these temperature data using an implicit solving scheme of the THEODOR code [2, 10], which is a 2D heat equation solver. Fig. 2(a) represent the photon flux as received by the cameras in a typical USN plasma.

The heat flux profiles data are collected along the yellow lines. The position of the lines are preserved for different discharges. At the outer target (right side), which consists in an

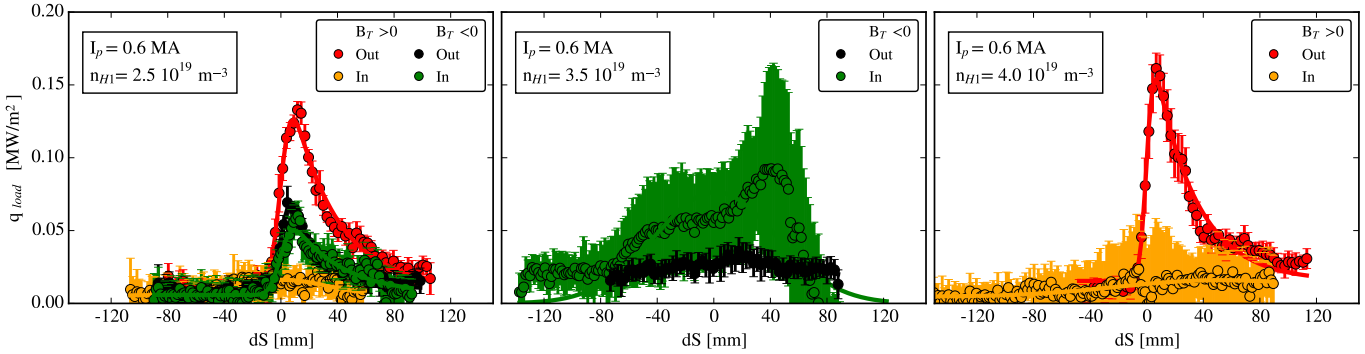

Figure 5: Heat flux deposition profiles as a function of the distance from the separatrix during the core plasma density scan with $I_p = 0.6$ MA.

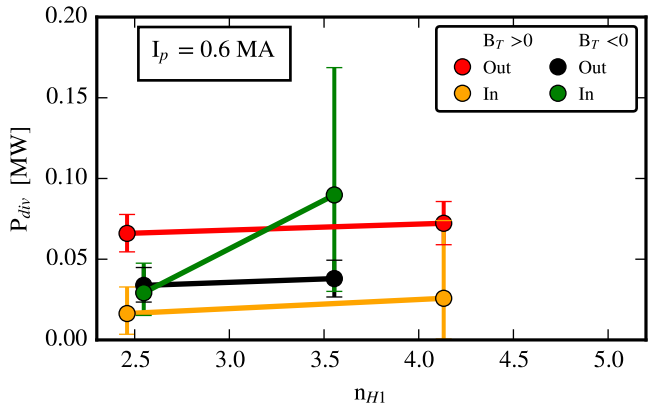

Figure 6: P_{div} as function of average core density, n_{H1}, for both toroidal field directions with $I_p = 0.6$ MA.

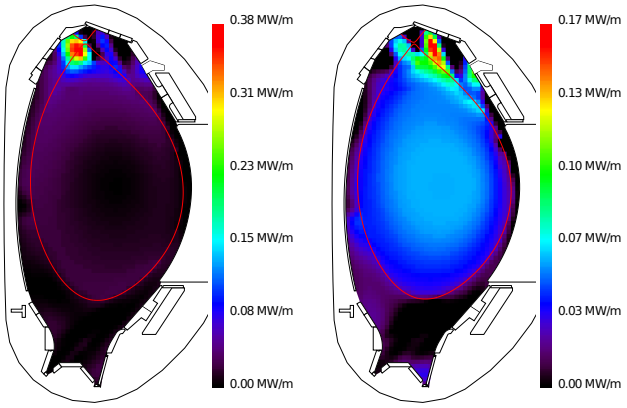

Figure 7: Tomographic reconstruction from bolometry of total radiation for (a) favourable toroidal field direction, $B_T > 0$, and (b) unfavourable toroidal field direction, $B_T < 0$.

special tile for IR measurements, the heat flux toroidally symmetric along the tile and, therefore, a single radial line can be used to characterise it. On the other hand, at the inner target (left side), the heat flux is localized toroidally and poloidally around the leading edge [11], which is a hotter, glowing region that receives larger heat loads due to geometrical effects (lack of tilt of the target components). The leading edge changes from one end of the tile to the other when the toroidal magnetic field and thus the helicity are reversed.

The lines of sight (LOS) of the bolometry system [12], which measure the power deposited by the incident electromagnetic radiation, are shown in Fig. 2(b). The tomographic reconstruction of these data can be used to analyse radiation patterns of the plasmas. The upper divertor of AUG has a small number of LOS available and thus the relative error (with respect to synthetic diagnostics based on the tomographic reconstructions) can be up to 30% with respect to the observed data. However, the overall radiation intensities and their positions are sufficiently reliable.

Langmuir probes are located in both targets and a strike point sweep (Fig. 2 (c)) was performed in order to obtain full profiles. Due to the lack of strike point control in the upper divertor, the plasma centre was displaced up and down by 2 cm, which caused the strike line to cross two different probes. A large divertor volume is desirable as more volumetric processes might occur. However, displacing the x-point further down would relegate most LPs to the private flux region (PFR) where their utility is limited.

Finally, for upstream characterization, Thomson scattering and lithium beam injection were used to obtain the upstream electron temperature and density profiles. Charge exchange recombination spectroscopy (CXRS) data are also available for most plasmas in Table 1.

3. Experimental Results

3.1. Core plasma density scan

The evolution of the profiles of the heat flux onto the targets with increasing core plasma density and $I_p = 0.8$ MA is presented in Fig. 3. The data are collected along the profile lines shown in Fig. 2 (a), as previously explained. Red and orange represent the favourable magnetic field direction, $B_T > 0$ or '+', while black and green represent the unfavourable direction, $B_T < 0$ or '-'.

In the transition from low to medium core density with $I_p = 0.8$ MA (Fig. 3) and $B_T > 0$, the heat flux onto the outer target does not change significantly ($\sim 5\%$) but the peak at the inner target is reduced $\sim 45\%$. In contrast, in the case of $B_T <$

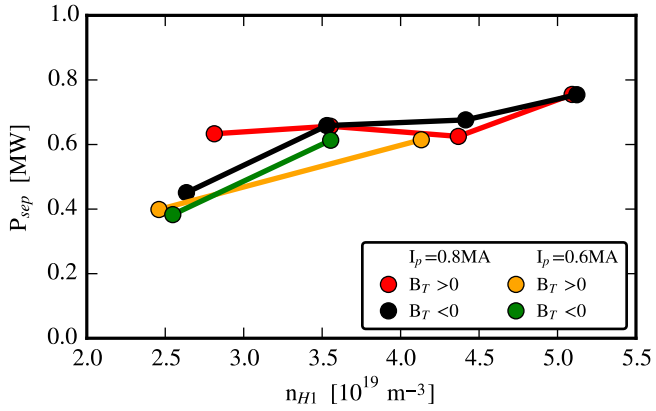

Figure 8: $P_{sep}(= P_{heating} - P_{rad,\rho<0.95})$ as function of core density, n_{H1} for different plasma currents and toroidal field directions.

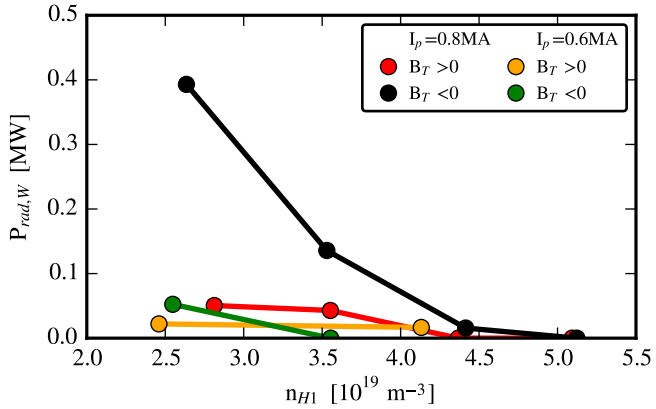

Figure 9: $P_{rad,W}$ as function of core density, n_{H1} for different plasma currents and toroidal field directions. $P_{rad,W}$ is estimated with a grazing incidence spectrometer for VUV.

0, the peak heat flux increase for both inner and outer target profiles by a factor ~ 2.4. At high density, the onset of power detachment is observed for both field directions at both targets because the peak heat flux drops to small values (measurement uncertainties are comparable to the magnitude of the signal).

In Fig. 4, the power to the divertor, $P_{div} = 2\pi\langle R\rangle \int q\, ds$ with $\langle R\rangle = 1.5\ m$ being the average major radius and q the heat flux density measured by the IR camera, is presented. The error bars correspond to the integral of upper and lower values of the uncertainty in the profiles of Fig 3. On top of that, the absolute value and the difference in/out might not be correct because toroidal symmetry cannot be assumed. Nonetheless, the trends for each divertor are more certain. P_{div} follows a similar trend (within uncertainties which are very large for high density cases) to that of the peaks of the heat flux profiles.

At a lower plasma current, $I_p = 0.6$ MA (Fig. 5), the inner target heat flux profile is already flat at low density for $B_T > 0$, indicating a power detached target. For the outer target, when the core density is increased from low to medium-high levels, the peak of the heat flux onto the outer target raises by a small amount, $\sim 20\%$. In the $B_T < 0$ direction, however, the onset of power detachment is triggered at the outer target because the peak of the heat flux in the medium density range drops by 50%, even as the value of P_{div} increases $\sim 5\%$ (Fig. 6). Although the heat flux increases along the entire profile at the inner target, the uncertainty of the measurements is considerable.

This apparent disparity of the effect of increasing plasma core density depending on the magnetic field direction is not a consequence of drifts exclusively. Considering the total heating power, $P_{heating} = P_{ohmic} + P_{ECRH}$, and the total radiated power in flux surfaces within $\rho_{pol} < 0.95$, $P_{rad,\rho<0.95}$, then the power crossing the serapatrix can be approximated by $P_{sep} = P_{heating} - P_{rad,\rho<0.95}$. In Fig. 8, it is shown that P_{sep} does not remain constant for different plasmas.

At medium current, $I_p = 0.8$ MA , P_{sep} values for both toroidal field directions are similar within the medium to medium-high density range. At high density, a 30% increase at high densities is observed for both field directions. However, at low density, P_{sep} for $B_T < 0$ is $\sim 30\%$ lower than for $B_T > 0$. Estimations of the tungsten core radiation are obtained with a grazing incidence spectrometer for VUV by calculating the fractional abundance of different tungsten ionisation states and the emissivity [13]. In Fig. 9, it is shown that $P_{rad,W}$ in unfavourable direction is up to a factor of ~ 5 larger than in favourable direction. The reason for this significant difference in tungsten radiation is yet to be understood.

Additionally, since radiation outside of the core increases with increasing core plasma density and most of it occurs within the inner divertor for $B_T > 0$ (Fig. 7), the stronger effect on the inner target with respect to the outer target may be partially explained.

For the cases at $I_p = 0.6$ MA , the amount of power crossing the separatrix is $\sim 30\%$ lower in the low density range than in the medium density range. However, in this case, the tungsten radiation is rather similar in both field directions. The 0.2 MW difference might be explained by the fact that, for those cases, $P_{ECRH} = 0.3$ MW instead of $P_{ERCH} = 0.5$ as for the rest of the database, as previously explained.

3.2. Plasma current scan

During the plasma current scan at low density, neither the peak heat flux (Fig. 10) nor the power onto both inner and outer targets (Fig. 11) did change significantly for $B_T < 0$ direction. On the other hand, for the $B_T > 0$ direction, the peak heat flux increased up to a factor of ~ 8 in the outer target and up to a factor of ~ 4 in the inner target. However, only the outer target P_{div} increases significantly across the entire scan (up to a factor of ~ 6).

In Fig. 12, the tungsten radiation is up to a factor of 6 higher in $B_T < 0$ direction with respect to $B_T > 0$ direction. This result is similar to the trend observed in the core plasma density scan. Because ohmic heating also increases with increasing plasma current, the resulting P_{sep} doesn't change within uncertainties. On the other hand, for $B_T > 0$, the small increase of tungsten radiation within the entire plasma current scan leads to doubling the amount of power crossing the separatrix. It should be noted again, that the low current, low density cases for both field directions had a reduce ECRH.

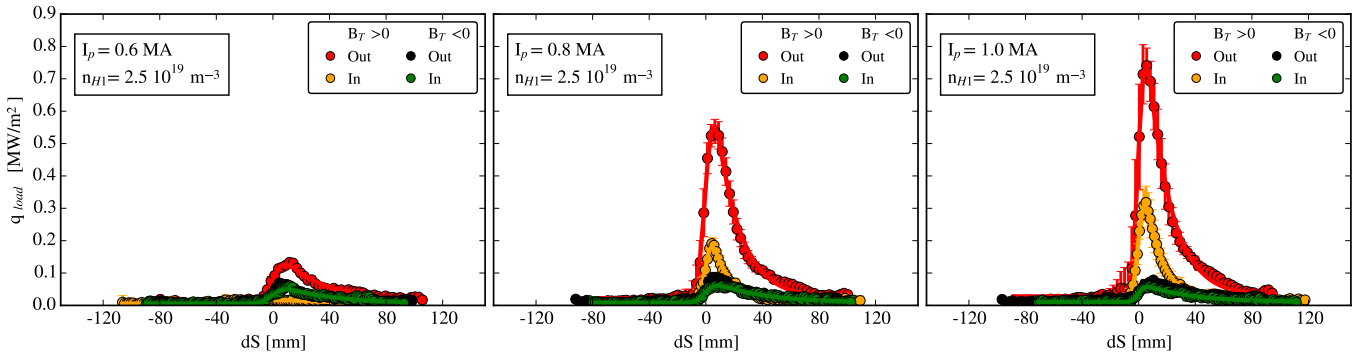

Figure 10: Heat deposition profiles as a function of the distance from the separatrix during the plasma current scan with $n_{H-1} = 2.5\ 10^{19}$ m^{-3}.

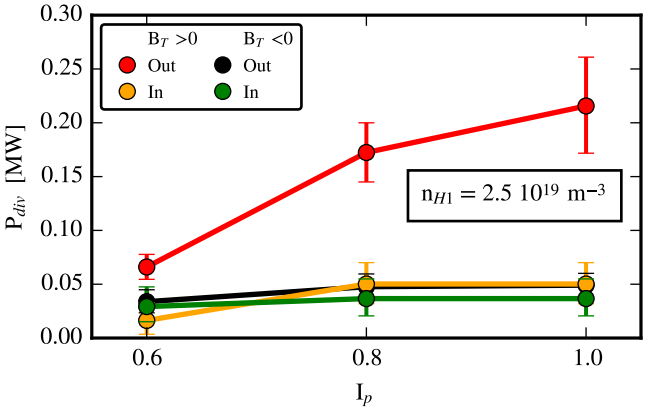

Figure 11: P$_{div}$ as function of plasma current, I_p, for both toroidal field directions with $n_{H1} = 2.5 \cdot 10^{19}$ m^{-3}.

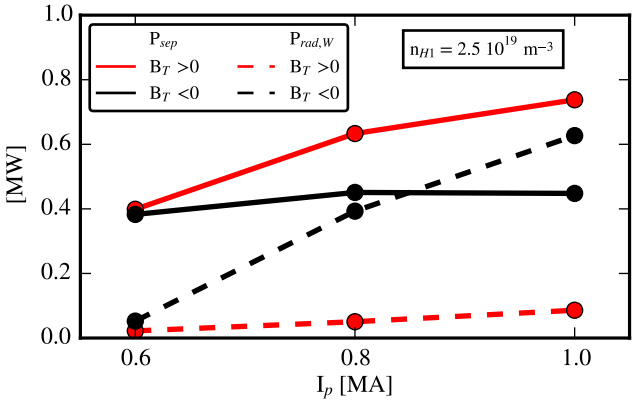

Figure 12: P$_{sep}$ (solid lines) and P$_{rad,W}$ (dashed lines) as function of plasma current, I$_p$, for both toroidal field directions with $n_{H1} = 2.5 \cdot 10^{19}$ m^{-3}.

3.3. Ion saturation current

The data of the ion saturation current measured by the Langmuir probes in the outer target for I$_p$ = 0.8 MA are presented in Fig. 13. The data have been taken from the entire strike point sweep, excluding events such as NBI blips or strong variation of density.

In the unfavourable direction, the peak of the ion saturation current increases by a factor of $\sim$ 2.5 when going from low to medium density. At high density, the peak of ion saturation current saturates and, at the highest density, it is reduced by a factor of $\sim$ 2.5, signalling the onset of particle detachment.

In the favourable field direction, the peak of the ion saturation current doubles in the transition from low to medium-high density but the onset of particle detachment is not observed.

In the plasma current scan (Fig. 14), the ion saturation current does not change significantly within statistical uncertainty for $B_T < 0$. On the other hand, for $B_T > 0$, the peak of the profile increases up to a factor of $\sim$ 6 at I$_p$ = 1.0 MA compared with I$_p$ = 0.6 MA.

The results of the ion saturation current measurements are in agreement with the trends of the IR data. Power detachment is apparently triggered at lower densities with respect to the onset of particle detachment.

4. Conclusions

As observed in previous studies, outer and inner target heat loads are more balanced in the unfavourable toroidal field direction with respect to the favourable field direction, in which the heat load to the outer target can be up to a factor of 4 larger than to the inner target.

At medium plasma current, increasing plasma core density affects the heat flux to the targets mainly in the unfavourable direction, while for favourable direction only a small reduction of the inner target heat flux is observed. For high densities, the onset of power detachment is observed in both targets for both field directions. In the density scan at low plasma current, the onset of power detachment is only observed at the outer target in the unfavourable direction at medium densities.

On the other hand, increasing plasma current also increases significantly the heat flux to the targets in the favourable field direction while the heat flux in the unfavourable direction remains unchanged within error bars.

This effect of the toroidal magnetic field direction on the evolution of the heat flux profiles is apparently not only an effect of drifts but it is also influenced by the power crossing the separatrix. This P$_{sep}$ is rather constant for medium to medium-high densities but different for most of the low density plasmas, except $B_T > 0$ with I$_p$ = 0.8 MA . These plasmas at low

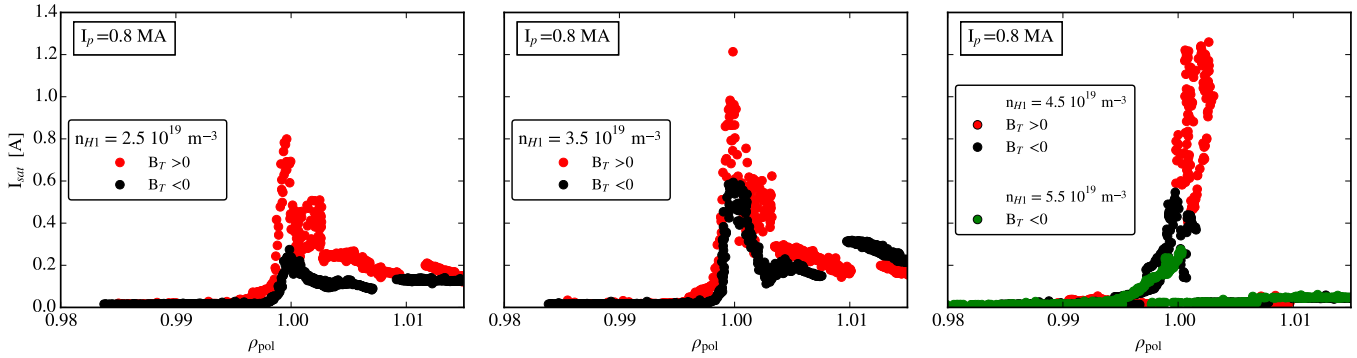

Figure 13: Ion saturation current profiles as a function of plasma core density, n_{H1}, for $I_p = 0.8$ MA.

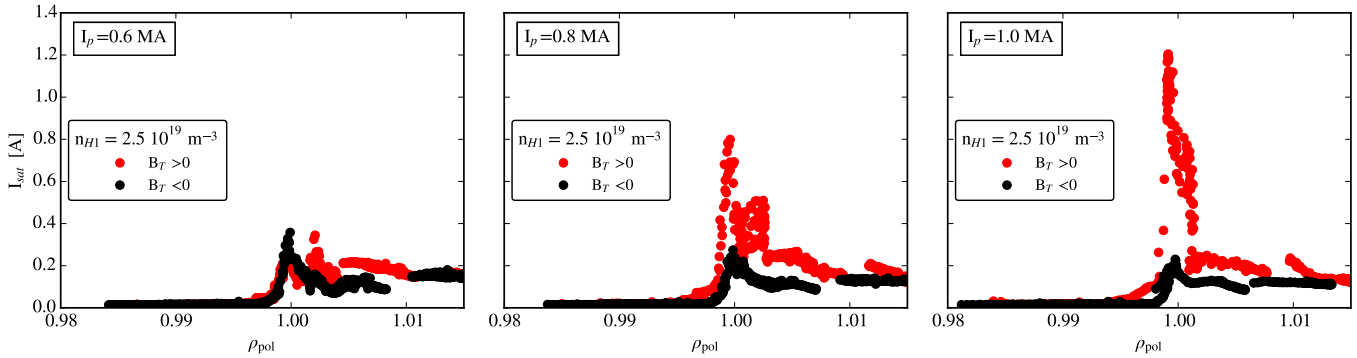

Figure 14: Ion saturation current profiles as a function of plasma current,I_p, for $n_{H1} = 2.5\ 10^{19}$ m^{-3}

density have a reduced P_{sep} due to two different issues: Tungsten radiation for $B_T < 0$ with $I_p = 0.8$ MA and lower ECRH power for $I_p = 0.6$ MA in both field directions. The tungsten core radiation in the unfavourable direction is, in general, much larger than in favourable direction, and this observation is not yet understood.

The ion saturation current data of the outer target show similar trends as those of the IR measurements. Particle detachment is only observed at the outer target in the unfavourable field direction for $I_p = 0.8$ MA. The onset of power detachment is triggered at a lower plasma core density than the onset of particle detachment, which is in line with observations of previous studies.

5. Acknowledgement

This work has been carried out within the framework of the EUROfusion Consortium and has received funding from the Euratom research and training programme 2014-2018 under grant agreement No 633053. The views and opinions expressed herein do not necessarily reflect those of the European Commission.

This work has been supported by the Academy of Finland, grant n. 285143.

6. Bibliography

[1] A. V. Chankin. Classical drifts in the tokamak SOL and divertor: models and experiment. *Journal of Nuclear Materials*, 241-243:199–213, 1997.

[2] A. Herrmann. Energy flux to the ASDEX-Upgrade diverter plates determined by thermography and calorimetry. *Plasma Physics and Controlled Fusion*, 37:17–29, 1995.

[3] M. Faitsch et al. Change of the scrape-off layer power width with the toroidal B-field direction ASDEX Upgrade. *Plasma Physics and Controlled Fusion*, 57:075005, 2015.

[4] B. Sieglin et al. Investigation of scrape-off layer and divertor heat transport in ASDEX Upgrade L-mode. *Plasma Physics and Controlled Fusion*, 58:055015, 2016.

[5] L. Aho-Mantila et al. Assesssment of SOLPS5.0 divertor solutions with drifts and currents against L-mode experiments in ASDEX Upgrade and JET. *Plasma Physics and Controlled Fusion*, 59:035003, 2017.

[6] A. V. Chankin et al. Influence of $E \times B$ drift in high recycling divertors on target asymmetries. *Plasma Physics and Controlled Fusion*, 57:095002, 2015.

[7] G. D. Porter et al. Detailed comparison of simulated and measured plasma profiles in the scrape-off layer and edge plasma of DIII-D. *Physics of Plasmas*, 7(9):3663–3680, 2000.

[8] N. Asakura. Field reversal effects on particle and heat fluxes in divertor on JT-60U. *Journal of Nuclear Materials*, 220-222:395–399, 1995.

[9] B. Sieglin et al. Real time capable infrared thermography for ASDEX Upgrade. *Review of Scientific Instruments*, 86:113502, 2015.

[10] D. Nille et al. Probabilistic inference of surface heat flux densities from infrared thermography. *A. Polpo et al. (eds.), Bayesian Inference and Maximum Entropy Methods in Science and Engineering, Springer Proceedings in Mathematics Statistics*, 239, 2018.

[11] M. Faitsch. *Infra Red Thermography Measurements for the Upper Divertor Target Plates in the ASDEX Upgrade Tokamak*. Master thesis. Universität Ulm, 2014.

[12] M. Bernert. *Analysis of the H-mode density limit in the ASDEX Upgrade tokamak using bolometry*. Master thesis. Ludwig-Maximilians-Universität München, 2013.

[13] T. Pütterich et al. Modelling of measured tungsten spectra from asdexupgrade and predictions for iter. *Plasma Physics and Controlled Fusion*, 50:085016, 2008.